# Nanoscale

## PAPER

Check for updates

# Synergistic 2D MoSe$_2$@WSe$_2$ nanohybrid hetero-structure toward superior hydrogen evolution and flexible supercapacitor†

Alkesh B. Patel, [ID] *‡$^{a,b}$ Jayraj V. Vaghasiya, [ID] ‡$^c$ Payal Chauhan, [ID] $^a$
C. K. Sumesh, [ID] $^d$ Vikas Patel,$^e$ Saurabh S. Soni, [ID] *$^c$ Kireetkumar D. Patel,*$^a$
Parveen Garg,$^f$ Gunvant K. Solanki$^a$ and Vivek M. Pathak$^a$

Two-dimensional (2D) transition metal dichalcogenide (TMDC) heterostructure is a new age strategy to achieve high electrocatalytic activity and ion storage capacity. The less complex and cost-effective applicability of the large-area TMDC heterostructure (HS) for energy applications require more research. Herein, we report the MoSe$_2$@WSe$_2$ nanohybrid HS electrocatalyst prepared using liquid exfoliated nanocrystals, followed by direct electrophoretic deposition (EPD). The improved catalytic activity is attributed to the exposure of catalytic active sites on the edge of nanocrystals after liquid exfoliation and the synergistic effect arises at HS interfaces between the MoSe$_2$ and WSe$_2$ nanocrystals. As predicted, the HS catalyst achieves a lower overpotential of 158 mV, a smaller Tafel slope of 46 mV dec$^{-1}$ for a current density of 10 mA cm$^{-2}$, and is stable for a long time. The flexible symmetric supercapacitor (FSSC) based on the HS catalyst demonstrates the excellent specific capacitance ($C_{sp}$) of 401 F g$^{-1}$ at 1 A g$^{-1}$, 97.20% capacitance retention after 5000 cycles and high flexible stability over 1000 bending cycles. This work presents a less complex and solution-processed efficient catalyst for future electrochemical energy applications.

## Introduction

Technology development for sustainable energy is needed to be explored due to the rapid consumption of fossil fuel and the hazards to the ecosystem due to the growing depletion of fossil fuels.[1] There are ways using which we can develop an ecofriendly technology for energy problems. First, hydrogen (H$_2$) and oxygen (O$_2$) production by electrocatalytic water splitting is an alternative method for sustainable energy reduces the utilization of fossil resources.[2,3] Second, supercapacitors

are the most promising energy storage devices with high power density, offering less environmental problems in comparison to dielectric capacitors, batteries, and fuel cells.[4] It is essential to develop low-cost and highly-stable photocathode that can efficiently undergo the water-splitting reactions for the high yield production of H$_2$ and O$_2$ and excellent power density with cyclic stability for energy storage.

Two-dimensional (2D) TMDCs have attracted most of the research on nanoelectronics and catalysis due to their intrinsic semiconducting characteristics and layer-dependent properties.[5,6-8] Among the TMDC family, 2D molybdenum diselenide (MoSe$_2$) and tungsten diselenide (WSe$_2$) are notable as they offer high carrier mobility, chemical stability, tunable bandgap, light–matter interaction, ambipolar characteristics, high current on/off ratios, and high electro/photocatalytic activity for photovoltaic, sensing, energy generation/storage, and optoelectronic applications.[9,10-12] In particular, their large specific surface areas, thermodynamically perfect energy band offset, and high density of active edge sites (Se facets) with low Gibbs free energy ($\Delta G_H$) make them a potential alternative to Pt-based precious metal electrocatalysts for HER reaction and supercapacitor applications.[13-15] Engineering the heterostructure between 2D materials are a novel strategy to boost the electronic and catalytic properties of the material.[16-18] Semiconducting heterointerfaces significantly enrich the charge/ion transfer rate by modulating the electronic state and induce a synergistic effect to facilitate the

$^a$*Department of Physics, Sardar Patel University, Shahid Chowk, Vallabh Vidyanagar, Anand 388 120, Gujarat, India. E-mail: patelalkesh51@yahoo.co.in, kdptflspu@gmail.com*

$^b$*Deparment of Paramedical Science, Charotar Institute of Paramedical Sciences, CHARUSAT Campus, Highway 139, Off. Nadiad-Petlad Road, Changa 388421, Gujarat, India*

$^c$*Department of Chemistry, Sardar Patel University, Vallabh Vidyanagar-388 120, Gujarat, India. E-mail: soni_b21@yahoo.co.in*

$^d$*Department of Physical Sciences, P. D. Patel Institute of Applied Science, CHARUSAT Campus, Highway 139, Off. Nadiad-Petlad Road, Changa 388421, Gujarat, India*

$^e$*Sophisticated Instrumentation Centre for Applied Research and Testing (SICART), Mota Bazaar, Vallabh Vidyanagar, Anand 388 120, Gujarat, India*

$^f$*UGC-DAE Consortium for Scientific Research, University Campus, Khandwa Road, Indore 452001, India*

‡Authors have contributed equally to this manuscript.

exposure of the active sites and capacitive behavior.[18–20] MoSe$_2$ and WSe$_2$ have minimal energy differences between the electronic states and similar lattice structure and constants, and hence are the most favorable choices for the heterostructure.[21] The epitaxial growth of the heterostructure by chemical vapor deposition (CVD) deals with costly sophisticated requirements, high temperature processing, and low yield. Considering this, solution processing of TMDC-based large-area heterostructure is the best alternative. Liquid-phase exfoliation technique (LPE) using ultrasonication affords high yield production of liquid-stabilized high-quality mono and multilayer TMDC nanocrystals, which is utilized in photonic and energy applications.[22] Drop casting, spin coating, and dip coating are the general deposition methods for liquid-exfoliated nanocrystals with several drawbacks such as limited control over the deposition area and thickness. In contrast, electrophoretic deposition (EPD) is the most effective technique for thin film preparation from colloidal suspension. EPD has advantages such as low-cost, easy implementation, homogeneous distribution, low-temperature processing, binder-free approach, thickness control, and reproducibility.[23,24] Ma *et al.* summarized that EPD is an effective and versatile deposition technique for exfoliated graphene and its composite for various applications.[25]

With reference to this prospective, a facile low-cost approach based on liquid-exfoliated nanocrystals, followed by electrophoretic deposition, is demonstrated to obtained large-area MoSe$_2$@WSe$_2$ HS. Morphological, compositional, and structural features of the MoSe$_2$@WSe$_2$ HS composite is confirmed by different physiochemical analysis. The effect of the HS interface is confirmed by the superior electrocatalytic performance of MoSe$_2$@WSe$_2$ HS for HER and supercapacitor application in comparison to the individual materials. The as-prepared MoSe$_2$/WSe$_2$ HS catalyst achieves a lower overpotential of 170 mV, smaller Tafel slope of 46 mV dec$^{-1}$ for the current density of 10 mA cm$^{-2}$, and is stable for a long time. FSSC fabricated using the MoSe$_2$@WSe$_2$ HS composite electrodes demonstrates excellent $C_{sp}$ of 401 F g$^{-1}$ at 1 A g$^{-1}$ and 97.20% capacitance retention after 5000 cycles. The FSSC also displays high stability over 1000 bending cycles.

# Experimental

## Materials

Molybdenum metal powder (99.9%), tungsten metal powder (99.9%), and selenium metal powder (99.9%) were purchased from Alfa Aesar. Glassy carbon substrate (3 mm thick) was purchased from Alfa Aesar, India. Carbon cloth was purchased from ACME research support Pte Ltd, Singapore. Other chemicals such as acetone, ethanol, poly(vinyl alcohol), and sulphuric acid were purchased form Hi-media Laboratories and used as received without further purification.

## Synthesis of MoSe$_2$ and WSe$_2$ nanocrystals

As shown in Fig. S1,† MoSe$_2$ and WSe$_2$ nanocrystals were synthesized by a direct liquid exfoliation method mentioned in our previously reported article.[23] In brief, 0.7 g bulk MoSe$_2$ and WSe$_2$ powder was well-ground in a mortar and dispersed in DMF at a concentration of 20 mg mL$^{-1}$. The mixture was sonicated in a bath sonicator at 40 kHz and 40% amplitude for 4 h. The prepared suspensions were centrifuged at 5000 rpm for 15 min for the removal of all the unexfoliated bulk. The stable colloidal suspension of MoSe$_2$ and WSe$_2$ were collected carefully for further characterization and electrode fabrication.

## Preparation of MoSe$_2$/CC, WSe$_2$/CC, and MoSe$_2$/WSe$_2$ HS/CC samples

The EPD deposition of liquid exfoliated nanocrystals is shown in Fig. 1. The hybrid colloidal suspension of the MoSe$_2$/WSe$_2$ nanocrystals was prepared by mixing MoSe$_2$ and WSe$_2$ nanocrystals suspensions with 1 : 1 (v/v) ratio. For the fabrication of the nanocrystal thin film by EPD, Al sheet and CC substrates separated by 1 cm were dipped into MoSe$_2$, WSe$_2$, and MoSe$_2$/WSe$_2$ nanocrystals' colloidal suspension. The constant DC voltage of +5 V was applied for 15 min for the uniform deposition of the nanocrystals' thin film. Then, the prepared electrodes were removed carefully and dried at 80 °C in a hot air oven for 4 h. The prepared samples were directly utilized for HER and supercapacitor application.
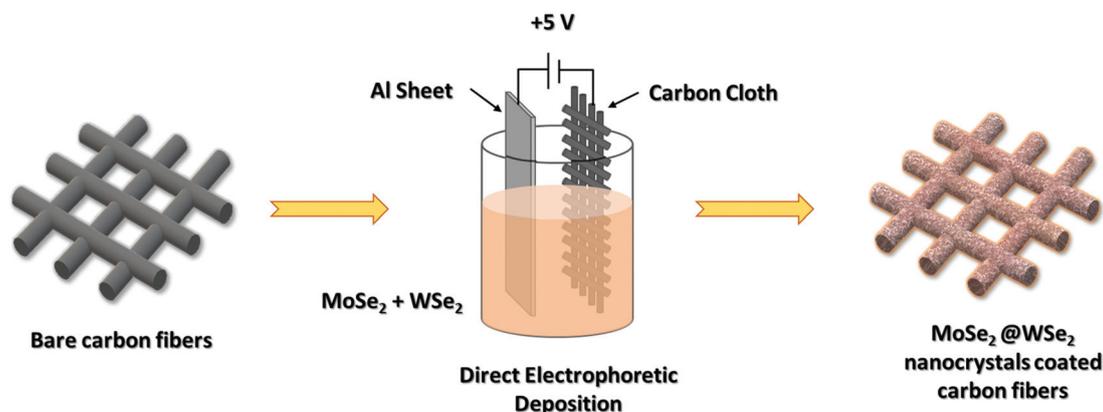


**Fig. 1** Direct EPD of MoSe$_2$@WSe$_2$ HS thin film on carbon cloth substrate.

## Preparation of poly(vinyl alcohol) (PVA)/sulfuric acid electrolyte

In a standard process, 1.0 g of PVA and 1.2 mL of $H_2SO_4$ (98 wt%) were introduced into 10 mL water. After this, the entire mixture was heated to 80 °C with constant magnetic stirring until the solution became transparent.

## Fabrication of an asymmetric flexible supercapacitor

Flexible supercapacitors were assembled in a stacked configuration with two similar electrodes (active area = 1.22 cm$^2$) of $MoSe_2$/$WSe_2$ HS/CC using a highly porous separator and PVA/$H_2SO_4$ as the electrolyte. The porous separator soaked in electrolyte was sandwiched between the two $MoSe_2$/$WSe_2$ HS/CC electrodes. A similar fabrication procedure follows in the preparation of $MoSe_2$- and $WSe_2$-based devices. The fabricated FSSCs are indicated by M||M, W||W, and MW||MW further in this article.

## Characterization and measurements

The morphological studies of the nanocrystals were made using high-resolution transmission electron microscopy (TEM, JEOL JEM 2100 microscope operated at 200 keV) and AFM (NT-MDT, Ntegra Aura). Micro-Raman spectra (Horiba XploRa Plus) was carried out at 532 nm wavelength excitation laser and UV-visible absorbance spectra (Optics, USB20000 + XR1-ES) were recorded in the wavelength range of 300–1000 nm for structural and optical confirmation. The microsurface morphology of the films on CC was initially characterized by field emission scanning electron microscopy (FESEM EDAX XL-30 Philips, Netherlands). The elemental composition was confirmed by energy dispersive analysis of X-ray and Auger Electron Spectroscopy Elemental mapping. The structural confirmation of the films examined by Micro Raman spectroscopy and standard X-ray diffraction (Bruker X-ray diffractometer with Cu Kα radiation, $\lambda$ = 1.5418 Å). X-ray photoelectron spectroscopy (XPS) data were collected on a SPECS ESCA system using Al Kα (1486.6 eV) X-ray source and a multichannel detector. The electrochemical activities were measured using a electrochemical workstation Matohm-PGSTAT204 (Autolab), Solartron 1287, CHI660E (CH instruments) in which the prepared electrodes, platinum wire, and Ag/Ag$^+$ are considered as the working, counter, and reference electrodes, respectively. Linear sweep polarization (LSV), cyclic voltammetry (CV), electrochemical impedance spectroscopy (EIS), and galvanostatic charging–discharging (GCD) analyses were used to examine the electrocatalytic performance of the prepared samples.

# Results and discussion

The morphological and structural properties of liquid-exfoliated $MoSe_2$ and $WSe_2$ nanocrystals were initially examined by TEM analysis. Fig. 2(a) and (b) depict the $MoSe_2$ and $WSe_2$ nanocrystals, respectively, on the HR-TEM grid with a lateral diameter in the nanometer scale. The HR-TEM images in

Fig. 2(c) and (d) show the vertically-aligned layered structure of the $MoSe_2$ and $WSe_2$ nanocrystals, respectively. The phase profile spectrum in Fig. 2(e) and (f) reveals the interplanar spacing of 0.645 nm and 0.647 nm, which corresponds to the (002) lattice plane of the hexagonal 2H-$MoSe_2$ and $WSe_2$, respectively.[26,27] The HR-TEM images in Fig. 2(g) and (h) demonstrate the interlayer lattice spacing. The $d$-spacing of 0.293 nm and 0.295 nm is noticed, as shown in Fig. 2(i) and (j), which is in good agreement with the (100) plane of 2H-$MoSe_2$ and $WSe_2$, respectively.[26,27] The 2H crystalline nature of $MoSe_2$-and $WSe_2$-exfoliated nanocrystals is confirmed by the selected area electron diffraction (SAED) pattern shown in Fig. 2(k) and (i). The morphology of $MoSe_2$ and $WSe_2$ nanocrystals was further characterized by AFM analysis.

Fig. S2(a) and (b)† display the isolated and uniform distribution of $MoSe_2$ and $WSe_2$ nanocrystals on the mica sheet. The step height profile in Fig. S2(c) and (d)† reveals the thickness of $MoSe_2$ and $WSe_2$ nanocrystals in the range of 20–50 nm suggested the multi-layered structure of the exfoliated nanocrystals. Moreover, the UV-visible absorption spectra of the $MoSe_2$ and $WSe_2$ nanocrystals suspension in Fig. S3† display the two broad absorption peaks for $MoSe_2$ at 691 nm and 801 nm, and $WSe_2$ at 566 nm and 769 nm, respectively, which is mainly attributed to the direct transition in the excitonic bands.[28] Raman spectroscopy and XRD were employed for the verification of the structural properties of the $MoSe_2$ and $WSe_2$ nanocrystals. Fig. 3(a) shows the XRD pattern of $MoSe_2$ and $WSe_2$ deposited on FTO substrate by EPD. The strong predominant peaks at 13.76° and 13.67° are produced by $WSe_2$ and $MoSe_2$, which can be assigned to the (002) lattice plane.[29,30] All other peaks are well indexed with no impurity peak, which confirmed the polycrystalline nature and mono-hexagonal phase of the as-prepared $MoSe_2$ and $WSe_2$ nanocrystals thin films (JCPDS# 29-0914 & JCPDS#38-1388). The broadening and weak intensity of the peaks indicates the nanocrystalline nature of exfoliated $MoSe_2$ and $WSe_2$. The XRD pattern of electrophoretically-deposited $MoSe_2$@$WSe_2$ on FTO and CC is shown in Fig. 3(b). Other than $MoSe_2$ and $WSe_2$, no extra peak or shifting in the peak is observed for $MoSe_2$@$WSe_2$ HS due to negligible lattice mismatch between $MoSe_2$ ($a$ = $b$ = 0.3288 nm and $c$ = 1.293 nm) and $WSe_2$ ($a$ = $b$ = 0.3282 nm and $c$ = 1.296 nm). $MoSe_2$@$WSe_2$/CC displays the diffraction peak at 13.80° and 31.20° corresponding to the (002) and (100) lattice plane of $MoSe_2$ and $WSe_2$, respectively. The other weak intensity peaks are not clearly identified due to a broad reflection peak at 25.2° corresponding to the (002) crystalline peak of graphite, which is characteristic of carbon-based materials. The Raman spectra of the $MoSe_2$, $WSe_2$, and $MoSe_2$@$WSe_2$ HS thin film on the FTO substrate is shown in Fig. 3(c). The three distinguished peaks of $MoSe_2$ are located at 242 and 172 cm$^{-1}$ for $A_{1g}$ out of plane, $E^1_g$ and $E^1_{2g}$ in plane vibration, respectively. For $WSe_2$, three peaks are located at 250 and 258 cm$^{-1}$, which are assigned to the $A^1_g$, $E^1_{2g}$, and 2LA(M) vibrational modes, respectively. In the Raman spectra of $MoSe_2$@$WSe_2$ HS, the characteristic peaks for $A_{1g}$, $E^1_g$, and $E^1_{2g}$ of $MoSe_2$, and $A^1_g$ and 2LA(M) of $WSe_2$ appear as a superposition. The
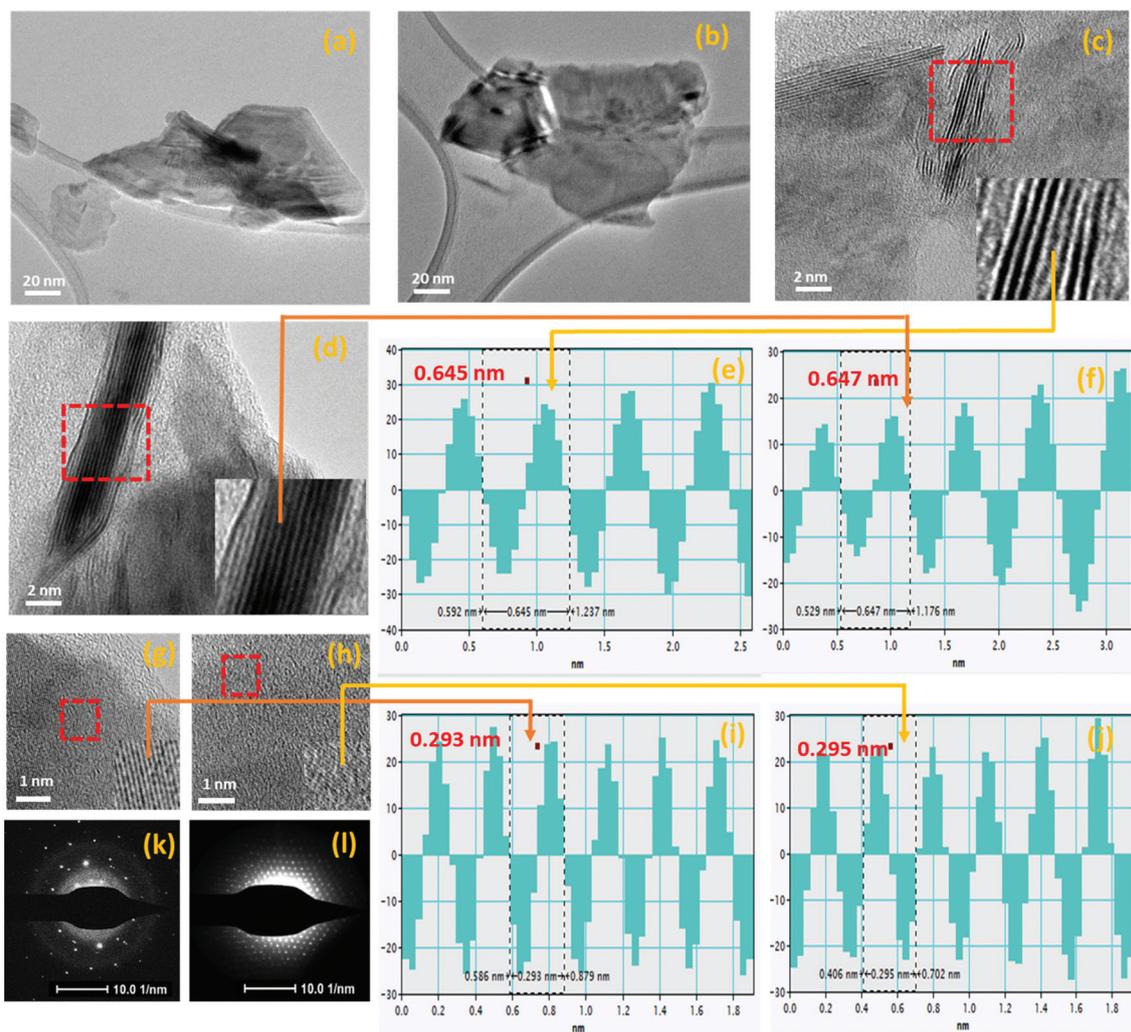
**Fig. 2** TEM micrographs-low magnification images of (a) $MoSe_2$ and (b) $WSe_2$ nanocrystals. The HR-TEM images of the layered structure of (c) $MoSe_2$ and (d) $WSe_2$, phase profile spectrum of the selected region of (e) $MoSe_2$ and (f) $WSe_2$. The HR-TEM images of the horizontally-grown (g) $MoSe_2$ and (h) $WSe_2$ with the inset magnified area under red line shows the lattice spacing, the corresponding phase profile spectrum of a selected region shows the lattice spacing of (i) 0.293 nm and (j) 0.295 nm for $MoSe_2$ and $WSe_2$, respectively, and the SAED pattern of (k) $MoSe_2$ and (l) $WSe_2$ nanocrystals.

intensity difference between the $MoSe_2$ and $WSe_2$ peaks indicates comparable interplanar interaction. However, the interplanar coupling remains weak due to the quasiplanar stacking of the nanocrystals.[31] In the Raman spectra of $MoSe_2@WSe_2$/CC, in Fig. 3(d), the peaks at about 1341 $cm^{-1}$ and 1589 $cm^{-1}$ responsible for the D and G bands, respectively, for the carbon originate from the vibrations of the $sp^2$ and $sp^3$ bonds of graphite.[32] The peaks corresponding to both $MoSe_2$ and $WSe_2$ are present as shown in the selected area plot, which confirm the heterogeneous deposition on the CC substrate. XPS analysis has been employed to probe the electronic state and binding energy of the heterostructure. The extended survey XPS spectrum of $MoSe_2@WSe_2$/CC HS confirmed the existence of both $MoSe_2$ and $WSe_2$ in the heterostructure composite. In Fig. 4(a), the Mo 3d spectra shows two peaks centered at 228.6 eV and 231.7 eV corresponding to Mo $3d_{5/2}$ and Mo $3d_{3/2}$,

respectively, for the Mo(IV) state.[33] The W spectra in Fig. 4(b) shows two peaks at 247.7 eV and 255.5 eV, which can be attributed to the W $4d_{5/2}$ and W $4d_{3/2}$ of the W(IV) state, respectively.[34] Fig. 4(c) displays the Se 3d peaks centered at 56.5 eV.[33] The surface morphology of carbon fibers (CFs) was investigated by SEM analysis. Fig. 5(a and b) display the smooth surface of bare CFs before EPD. After EPD, continuous nanocrystal deposition can be observed over a surface of CFs, as shown in Fig. 5(c and d). Fig. 5(e) shows the single CF fully covered by the nanocrystals, which suggests the uniform deposition of nanocrystals on every CF. Fig. 5(f) shows the deposited nanocrystals at high magnification, demonstrating the randomly oriented nanocrystals with sharp edges after exfoliation, which can serve as a catalytically active site for $H_2$ production. The elemental mapping images recorded from the surface of single CF are depicted in Fig. 5(g–j), which demon-
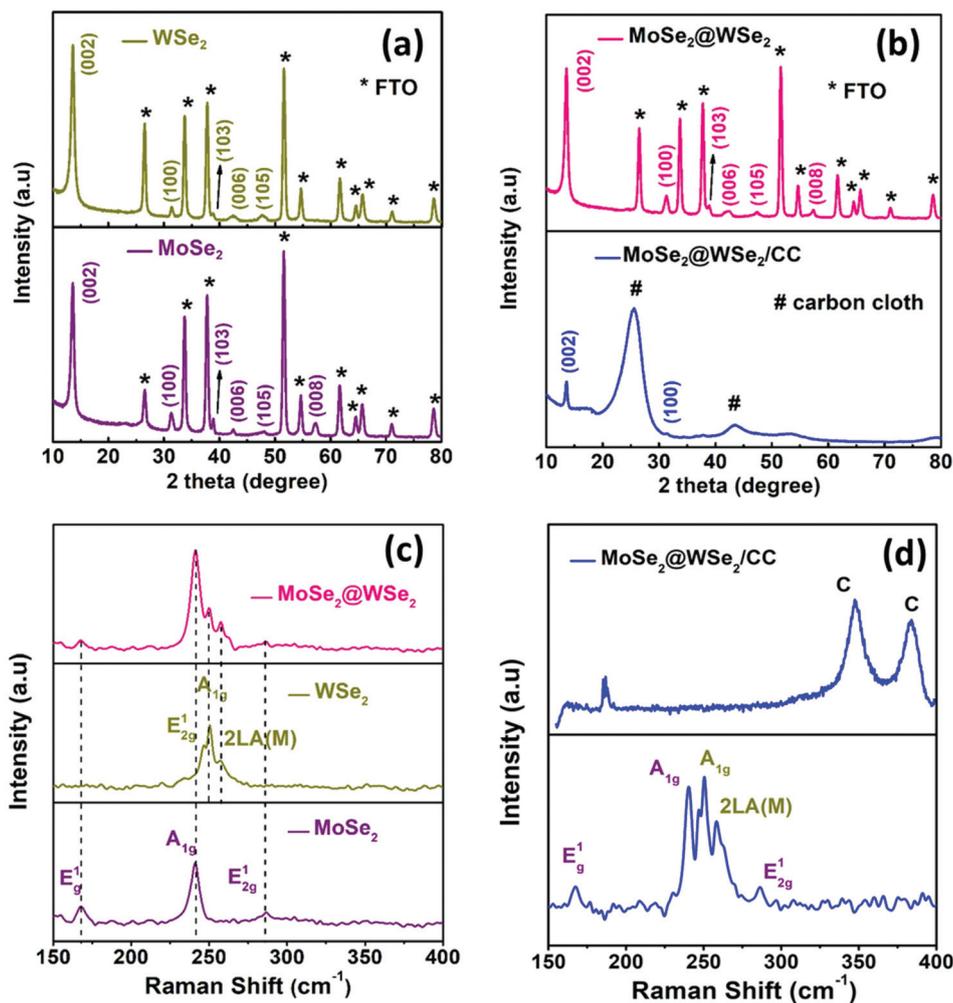
**Fig. 3**  XRD pattern (a) $WSe_2$ and $MoSe_2$ (b) $MoSe_2@WSe_2$/FTO and $MoSe_2@WSe_2$/CC. Raman spectra (c) $WSe_2$ and $MoSe_2$ (d) $MoSe_2@WSe_2$/FTO and $MoSe_2@WSe_2$/CC.
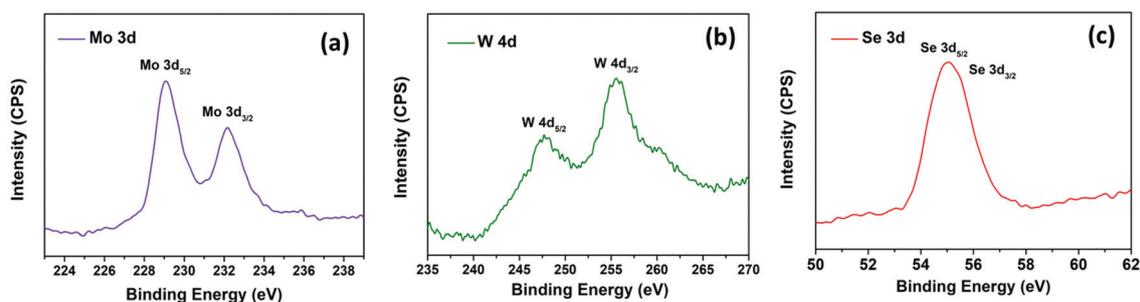


**Fig. 4**  XPS spectra of $MoSe_2@WSe_2$/CC (a) Mo 3d core level peaks region spectrum, (b) W 4d core level peaks region spectrum, (c) Se 3d core level peaks region spectrum.

strated the continuous distribution and co-existence of Mo, W, and Se elements, thus confirming the heterogeneous deposition of $MoSe_2$ and $WSe_2$ nanocrystals. The corresponding EDAX spectra shown in Fig. S4† demonstrate the slightly diminished emission peaks of Mo, W, and Se due to the large emission peak of carbon of the CC substrate. The results from

the above-mentioned analyses confirm the successful formation of the $MoSe_2@WSe_2$ HS composite layer on the CC substrate.

The electrocatalytic HER performance of the prepared $MoSe_2$/CC, $WSe_2$/CC, and $MoSe_2@WSe_2$/CC electrodes were investigated in the acidic electrolyte of 0.5 M $H_2SO_4$. Fig. 6(a)
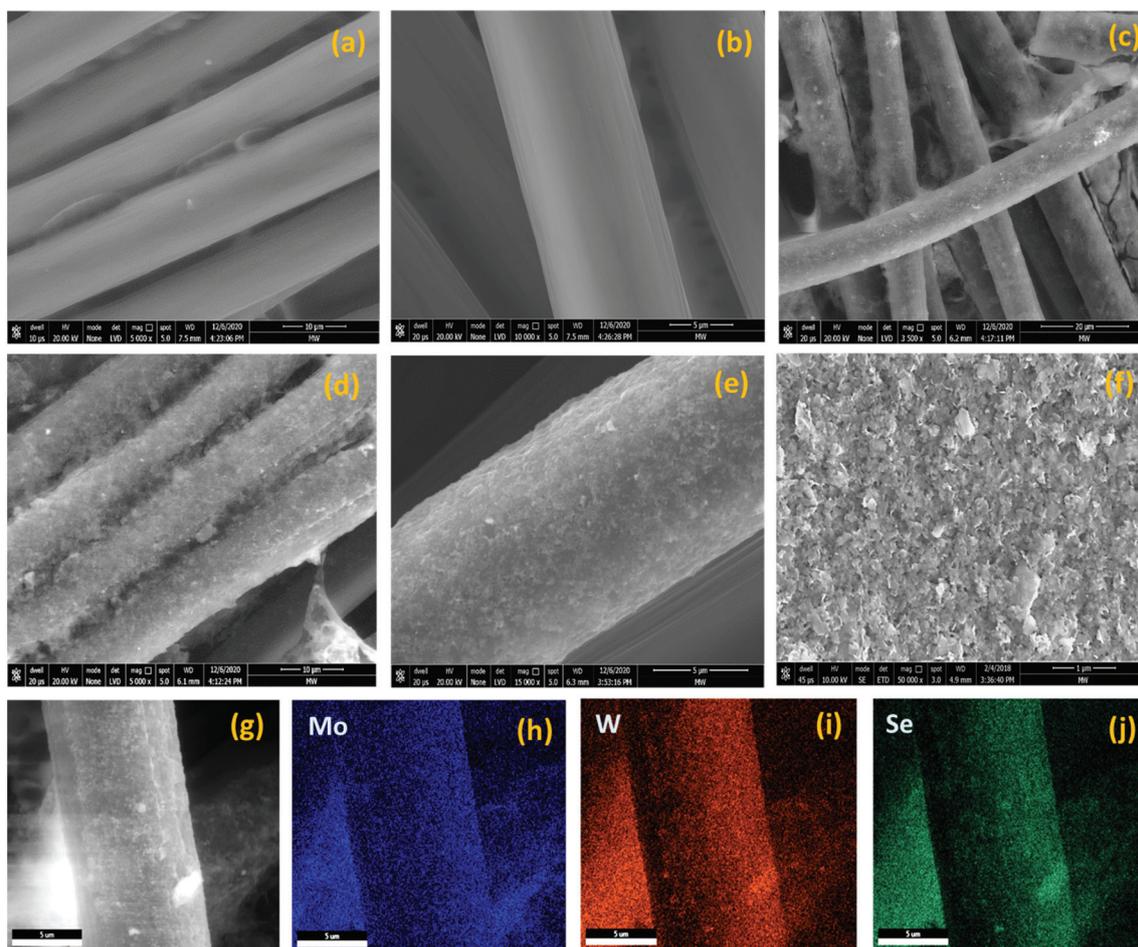
**Fig. 5** (a) The schematic illustration of MoSe$_2$@WSe$_2$ HS film deposition on carbon fiber cloth by EPD. SEM images of (b and c) bare carbon fibers and (d and e) MoSe$_2$@WSe$_2$ HS-coated carbon fibers. (f–j) EDAX elemental mapping of MoSe$_2$@WSe$_2$ HS on single CF.

depicts the LSV curves recorded at room temperature in the potential range from −0.35 V to 0.1 V at a scan rate of 10 mV s$^{-1}$, revealing the smaller onset potential of MoSe$_2$@WSe$_2$/CC than MoSe$_2$/CC and WSe$_2$/CC. MoSe$_2$/CC and WSe$_2$/CC exhibit an approximate overpotential of 177 mV and 220 mV, respectively, for a current density of 10 mA cm$^{-2}$. In the case of MoSe$_2$@WSe$_2$/CC, the overpotential decreases up to 158 mV for the current density of 10 mA cm$^{-2}$, demonstrating superior catalytic activity in comparison to the individual materials' electrode. The reasons that may be responsible for the improved performance of the heterostructure are: (i) exposure of the catalytically active site on the edge of the nanocrystals after liquid exfoliation as shown in Fig. 3(f),[37] (ii) the carbon-based substrate serves as a highly conductive carbonaceous support to nanostructured HER catalyst for fast electron transfer,[38] (iii) synergistic effect of MoSe$_2$@WSe$_2$ HS also significantly boosts the HER kinetics.[39] The HER activity can be further evaluated by the Tafel plot extracted by the corresponding LSV curves. The Tafel slopes can be obtained from the linear portions of the plots using the Tafel equation $\eta = b \log(j) + a$, where $\eta$ is the overpotential, $b$ is the Tafel slope,

and $j$ represents the current density.[40] Fig. 6(b) demonstrates that MoSe$_2$@WSe$_2$/CC achieves a Tafel slope of 46 mV dec$^{-1}$, which is much lower than that of MoSe$_2$/CC (78 mV dec$^{-1}$) and WSe$_2$/CC (88 mV dec$^{-1}$), indicating the rapid electron transfer mechanism in the HS catalyst. The Tafel slopes also reveal that the following Volmer–Heyrovsky mechanism is behind the HER kinetics.[41]

$$H^+ + e^- \rightarrow H* \quad \text{(Volmer reaction)} \qquad (1)$$

$$H* + H^+ + e^- \rightarrow H_2 \quad \text{(Heyrovsky reaction)} \qquad (2)$$

Electrochemical impedance spectroscopy (EIS) was carried out to further investigate the HER kinetics of the prepared electrodes in the frequency range from 0.01 Hz to 1 MHz under dark at a bias voltage of 200 mV. The Nyquist plots of MoSe$_2$/CC, WSe$_2$/CC, and MoSe$_2$@WSe$_2$/CC in 0.5 M H$_2$SO$_4$ are depicted in Fig. 6(c). The semicircle intercept at $x$-axis near the origin determined the series resistance ($R_s$) related to the internal resistance of the electrochemical system. The arc diameter of the semicircle at the low-frequency range indicates the charge transfer resistance ($R_{ct}$) at the catalyst/electrolyte
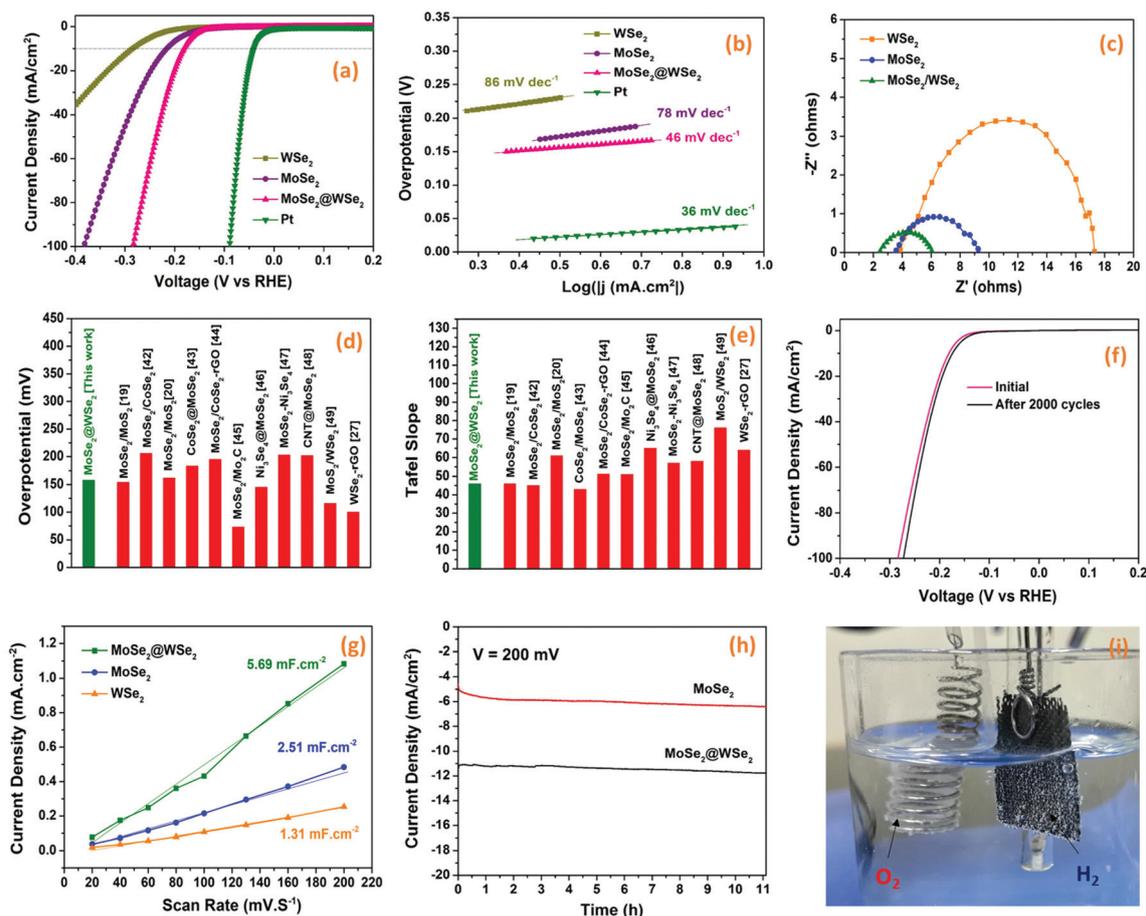
**Fig. 6** (a) LSV polarization curves, (b) Tafel plots, (c) EIS curves of $MoSe_2$, $WSe_2$, and $MoSe_2@WSe_2$/CC HS electrodes. A comparative plot of (d) overpotential and (e) Tafel slope for $MoSe_2@WSe_2$ HS with other composite catalysts. (f) Initial and after the 2000th cycle, the polarization curves of the $MoSe_2@WSe_2$ HS electrode. (g) The capacitive current density at a different scan rate of $MoSe_2$/CC, $WSe_2$/CC, and $MoSe_2@WSe_2$/CC electrodes. (h) Chronoamperometric curves of $MoSe_2$/CC and $MoSe_2@WSe_2$/CC electrodes. (i) The digital photograph of the $MoSe_2@WSe_2$ HS electrode during chronoamperometry measurement.

interface. The smaller values of $R_s$ for all the samples indicates the strong adhesion of EPD-deposited nanocrystals films on the CC substrate, which significantly reduces the contact resistance.[42] $MoSe_2$/CC and $WSe_2$/CC possess $R_{ct}$ values of 5.76 $\Omega$ cm$^2$ and 13.40 $\Omega$ cm$^2$, while $MoSe_2@WSe_2$/CC show 3.60 $\Omega$ cm$^2$. In comparison, the smallest $R_s$ and $R_{ct}$ values of the heterostructure composite indicate better electronic conductivity and low interfacial resistance at the catalyst/electrolyte interface.[43] M–S analysis was conducted to investigate the influence of the heterostructure on the semiconductor/electrolyte interface. The positive slope of the plots in Fig. S5† indicates the n-type semiconductor properties of the samples. According to M–S analysis, the flat band potential (EFB) for an n-type semiconductor lies near the conduction band of the semiconductor. The EFB of $MoSe_2$, $WSe_2$, and $MoSe_2@WSe_2$ HS is estimated from the x intercepts of the linear region of the M–S plots. The EFB of $MoSe_2@WSe_2$ HS is −1.44 V with a negative shift of 0.3 V in comparison to $WSe_2$. The upward shift in the EFB and a smaller slope indicate efficient charge transfer at the semiconductor/electrolyte interface, which

further confirmed the formation of a heterostructure.[35,36] The comparison data plot of overpotential and Tafel slope with some $MoSe_2$- and $WSe_2$-based composites is depicted in Fig. 6(d) and (e).[19,20,27,44–51] The long-term stability is a crucial factor to examine the practical application of the catalysts for HER activity. Fig. 6(f) depicts the polarization curve of the $MoSe_2@WSe_2$/CC electrode at a scan rate of 25 mV s$^{-1}$, showing the marginal change in the current density and overpotential even after 2000 cycles of LSV, indicating its robustness and durability in acidic medium. Fig. S6(a)† shows the LSV curves of bulk- and nanocrystal-based $MoSe_2@WSe_2$ HS in 0.5 M $H_2SO_4$, demonstrating higher electrocatalytic activity of the exfoliated HS composite. We further estimated the electrochemically active surface area (ECSA) by recording a series of cyclic voltammetric measurements in the potential range of 0.15 V–0.35 V (vs. RHE) at different scan rates from 10 mV s$^{-1}$ to 250 mV s$^{-1}$. The CV curves of $MoSe_2$/CC, $WSe_2$/CC, and $MoSe_2@WSe_2$/CC at various scan rates is shown in Fig. S6(b–d).† The $C_{dl}$ value is equivalent to the slope of the plot $\Delta j$ ($j_a$ − $j_c$) vs. the middle potential (0.25 V) as a function of scan rate,

as shown in Fig. 6(g). MoSe$_2$@WSe$_2$/CC has a $C_{dl}$ value of 5.69 mF cm$^2$, which is 2.26 times and 4.34 times higher than that of MoSe$_2$/CC (2.51 mF cm$^2$) and WSe$_2$/CC (1.31 mF cm$^2$), respectively, indicating the large exposure of the catalytically active surface area of the HS catalyst, which supports the superior HER performance.[52] The continuous hydrogen evolution was assayed by chronoamperometry measurement ($j$–$t$). The chronoamperometric curve of MoSe$_2$/CC and MoSe$_2$@WSe$_2$/CC at the overpotential of $\eta$ = 200 mV for 12.5 h is shown in Fig. 6(h). The pure MoSe$_2$/CC has severely low HER activity in comparison to that of MoSe$_2$@WSe$_2$/CC under the same bias conditions. The digital photograph in Fig. 6(i) shows vigorous H$_2$ bubble generation on the surface of the MoSe$_2$@WSe$_2$ HS/CC electrode and O$_2$ formation at the Pt wire electrode at 12 h (ESI Movie†). Overall, the smaller overpotential, lower Tafel slope and charge transfer resistance, and higher double layer capacitance signify the superior HER performance of the HS catalyst in comparison to the individual catalyst. The excellent stability toward the long term HER

activity makes the MoSe$_2$@WSe$_2$ HS composite a promising catalyst for future practical electrochemical applications.

### Flexible supercapacitor performance analysis

The all-solid-state flexible supercapacitors is the future of light-weight wearable electronics owing to the several advantages, such as safety, flexibility, stability, and easy fabrication. The electrochemical energy storage properties of the MoSe$_2$@WSe$_2$ HS composite were studied by assembling a flexible symmetric supercapacitor (FSSC), as shown in Fig. 7(a). The device fabrication detail procedure is shown in the ESI experimental section.† The voltammetric performance of M||M, W||W, and MW||MW FSSCs under the same scanning rate of 100 mV s$^{-1}$ with an operating window from 0 to 1 V is shown in Fig. 7(b). All the CV curves demonstrate a relatively rectangular shape and good reversibility. In comparison, the MW||MW FSSC displays a broader CV curve, which reveals the pure and superior pseudocapacitive behavior than that of the M||M and W||W FSSC devices. Furthermore, a systematic study of MW||MW
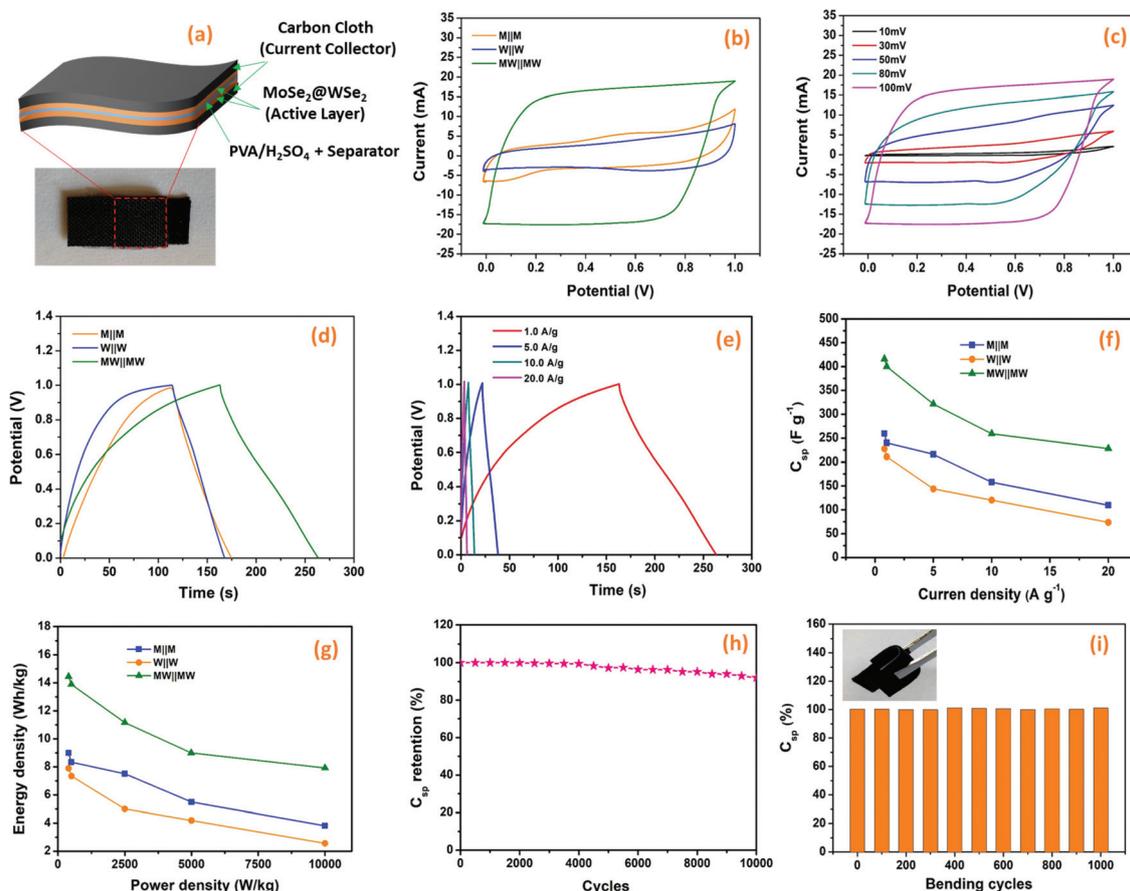


**Fig. 7** Energy storage study; (a) The schematic diagram and digital photograph of the prepared FSSC, (b) typical CV plots of M||M, W||W and MW||MW FSSCs at scan rate of 100 mV s$^{-1}$, (c) CV curves of MW||MW FSSC at different scan rates, (d) typical galvanostatic charge–discharge plots of the M||M, W||W, and MW||MW FSSCs at a current density of 0.8 A g$^{-1}$, (e) The $C_{sp}$ of M||M, W||W, and MW||MW FSSCs as a function of the current density, (f) GCD plots of MW||MW FSSCs at different current densities, (g) Ragone plot (energy density *versus* power density) for M||M, W||W, and MW||MW FSSCs, (h) cycling stability of MW||MW FSSC over 10,000 cycles, and (i) flexibility study (bending) of MW||MW FSSC at a current density of 1 A g$^{-1}$ (the inset image of flexible MW||MW FSSC).

FSSC was performed by recording the CV plots at different scan rates of 10–100 mV s$^{-1}$, as shown in Fig. 7(c). The area of the CV curve increases with the increasing scan rate by maintaining the symmetrical shape, illustrating the rapid transfer of electrolyte ions and good reversible faradaic pseudocapacitive nature of the MW||MW FSSC device. The further determination of the capacitive behavior was undertaken by galvanostatic charge and discharge (GCD) plots. For comparison, the GCD plots of all the FSSCs devices in the potential range of 0–1 V at a current density of 0.8 A g$^{-1}$ is depicted in Fig. 7(d). The symmetrical charging/discharging curves reflecting a high capability and reversible behavior of all the three FSSCs devices.[53] The non-linear nature of the GCD demonstrates the high redox reactions and faradaic pseudocapacitive behavior of the composite materials.[54] The MW||MW FSSC possesses a longer charging/discharging curve, indicating the superior charge-storage capacity and better supercapacitor performance in comparison to individual material-based FSSC devices. The GCD plot of MW||MW FSSC at different current densities of 1 to 20 A g$^{-1}$ is depicted in Fig. 7(e). The GCD plots almost maintained a similar triangular shape in the potential range of 0 to 1 V, suggesting the sustainable capacitance behavior of the device in a broad current range. The gravimetric specific capacitance ($C_{sp}$, F g$^{-1}$), power density ($P$, W kg$^{-1}$), and energy density ($E$, W h kg$^{-1}$) can be obtained from the GCD curves with the following equations[55]

$$C_{sp} = 4 \times I \times \Delta t / m \times \Delta V \tag{3}$$

$$E = \frac{C_s (\Delta V)^2}{4 \times 2} \tag{4}$$

$$P = \frac{E}{\Delta t} \tag{5}$$

where $I$ represents the current density (mA), $\Delta t$ denotes the discharge time (s), $m$ is the total mass of both the electrodes (g), and $\Delta V$ is the discharge voltage (V). The $C_{sp}$ values as a function of different current density for all three FSSC devices are demonstrated in Fig. 7(f). The calculated $C_{sp}$ of MW||MW FSSC was 401 F g$^{-1}$ at a current density of 1.0 A g$^{-1}$, much higher than that of M||M FSSC (240 F g$^{-1}$) and W||W FSSC (211.2 F g$^{-1}$). The improved capacitance behavior of MW||MW FSSC can be attributed to the synergistic effect of large area MoSe$_2$@WSe$_2$ HS, which promotes ion-transfer and density of the catalytic reaction sites to enhance the efficiency of redox reactions at the solid–liquid interface.[19,56] Moreover, MW||MW FSSC achieves $C_{sp}$ values of 416, 401, 321, 259, and 228 F g$^{-1}$ at the current densities of 0.8, 1, 5, 10, and 20 A g$^{-1}$, respectively, which are more than two-folds higher compared to both M||M FSSC and W||W FSSC. The $C_{sp}$ value drops with the increase in the current density because of the small charging and discharging time is attributed to the time and concentration constraints of hydrogen and oxygen atoms to react with the active material at a higher current density. It is noticeable that MW||MW FSSC maintained 54.80% capacitance when the current density increased by 25 times, demonstrating the excellent kinetic performance of the device. The power

density ($p$) and energy density ($E$) are crucial factors to evaluate the performance of the supercapacitor. The extracted Ragone plot (power density ($p$) vs. energy density ($E$)) for all the three FSSC devices is shown in Fig. 7(g). At the current density of 0.8 A g$^{-1}$, the maximum procurable value of $E$ is 14.44 W h kg$^{-1}$ is obtained at a $P$ of 397 W kg$^{-1}$, and 8.1 W h kg$^{-1}$ can be maintained even at a higher $P$ of 9987 W kg$^{-1}$ for MW||MW FSSC. Meanwhile, M||M and W||W FSSCs showed the maximum energy density of 9.13 W h kg$^{-1}$ and 7.88 W h kg$^{-1}$ at a power density of 397 W kg$^{-1}$, which denotes the improved and admirable supercapacitor performance of the HS composite. Further, the interfacial charge kinetic mechanism of the fabricated FSSCs was investigated by electrochemical impedance spectroscopy (EIS). The Nyquist plots of all the three FSSC devices were recorded using 10 mV AC amplitude and the frequency range of 0.01 Hz to 1 MHz is presented in Fig. S7.† The ESR (equivalent series resistance, $R_s$) related to the internal resistance and electron conductivity can be determined by the intersection of the plot on the real axis at a high-frequency range.[57] As illustrated in the enlarged EIS curve, the MW||MW FSSC displayed the lowest ESR with an $R_s$ value of 2.63 Ω in comparison to M||M (3.42 Ω) and W||W (3.7 Ω) FSSC. The diffusion resistance ($R_w$) can be obtained from the slope of the linear portion at the low-frequency region.[57] Among all, the MW||MW FSSC possesses a smaller ESR and higher slope of the Nyquist plot, further demonstrating its higher electron conductivity and better capacitance nature for promoting the diffusion of the ions at solid–liquid interface. The enhanced electrical conductivity and ion diffusion rate are manifested by the synergetic effect of the MoSe$_2$@WSe$_2$ HS composite electrodes, which lead to the superior capacitance performance of the MW||MW FSSC. The cycling durability of the MW||MW FSSC is a crucial factor for its realistic use, which was indicated by the $C_{sp}$ calculated under the 10 000 GCD cycles (Fig. 7(h)) with the high current density of 20 A g$^{-1}$. The $C_{sp}$ slightly decreased from 228 F g$^{-1}$ to 221.61 F g$^{-1}$ after 5000 cycles, which represents 97.20% retention of the initial value. On the other hand, there was 91.94% capacity retention after 10 000 cycles, suggesting the excellent cycling stability of MW|| MW FSSC. To determine the flexibility of the fabricated MW|| MW FSSC, the $C_{sp}$ calculated was evaluated using GCD measurement under 1000 bending cycles at a bending angle of 180°. Fig. 7(i) indicates that after various bending cycles, there is no major impact on the capacitive performance of the device. It demonstrated that the fabricated FSSC based on the MoSe$_2$@WSe$_2$ HS composite has excellent flexibility to be easily integrated into various portable and wearable electronics. Table 1 depicts the comparative data of some recently reported flexible supercapacitor based on TMDC composite electrodes. The results mentioned above support EPD as a reliable method to obtained compact and homogeneous deposition of liquid-exfoliated nanocrystals. The working mechanism of MoSe$_2$@WSe$_2$ HS-based hydrogen evolution and FSSC is schematically illustrated in Fig. 8(a and b).

The nanocrystal nature and synergistic effect of MoSe$_2$@WSe$_2$ HS provide catalytically active sites on the edges,

**Table 1** Comparative data based on different composite electrodes for flexible supercapacitors

| Flexible device | Electrolyte | Energy density (W h kg$^{-1}$)/power density (W kg$^{-1}$) | Retention (%) | Specific capacitance (F g$^{-1}$) | Ref. |
|---|---|---|---|---|---|
| MoSe$_2$ NF//MoSe$_2$ NR | PVA/KOH | 36/1400 | 92/2000 | 133 | 53 |
| NiCoP@MoSe$_2$//AC | PVA/KOH | 55.1/799.8 | 95.8/8000 | 155 | 56 |
| VS2//VS2 | PVA/LiClO$_4$ | 25.9/6200 | 89/6000 | 118 | 58 |
| WS$_2$@CNT//WS$_2$@CNT | PVA/H$_2$SO$_4$ | 0.0798 mW h cm$^{-2}$/5.745 mW cm$^{-2}$ | 76.88/10 000 | 574.65 mF cm$^{-2}$ | 59 |
| Co$_3$S$_4$/WS$_2$//Co$_3$S$_4$/WS$_2$ | PVA/H$_2$SO$_4$ | 10.17/6700 | 92/2000 | 339 | 54 |
| Mo–doped Co$_9$S$_8$//AC | PVA/KOH | 14/369 | 80.07/30 000 | 37.37 | 60 |
| CoS$_2$//N doped carbon | PVA/KOH | 3.16 mW h cm$^{-3}$/37.2 mW cm$^{-3}$ | 86.2/16 000 | 28.7 | 61 |
| 1T WTe$_2$//1T WTe$_2$ | PVA/H$_3$PO$_4$ | 31/7800 | 91/5500 | 221 | 62 |
| MnSe MF//MnSe MF | PVA/LiCl | 55.42/894.25 | 97.15 /5000 | 200 | 63 |
| MoSe$_2$/MWCNTs//MoSe$_2$/MWCNTs | PVA/KOH | 7.41/681 | 96/1000 | 27.24 | 64 |
| MoS$_2$/KB//NiCo$_2$O$_4$ | PVA/KOH | 25.7/779.9 | 91/5000 | 72 | 65 |
| MoSe$_2$@WSe$_2$//MoSe$_2$@WSe$_2$ | PVA/H$_2$SO$_4$ | 14.44/397 | 91.94/10 000 | 416 | This work |
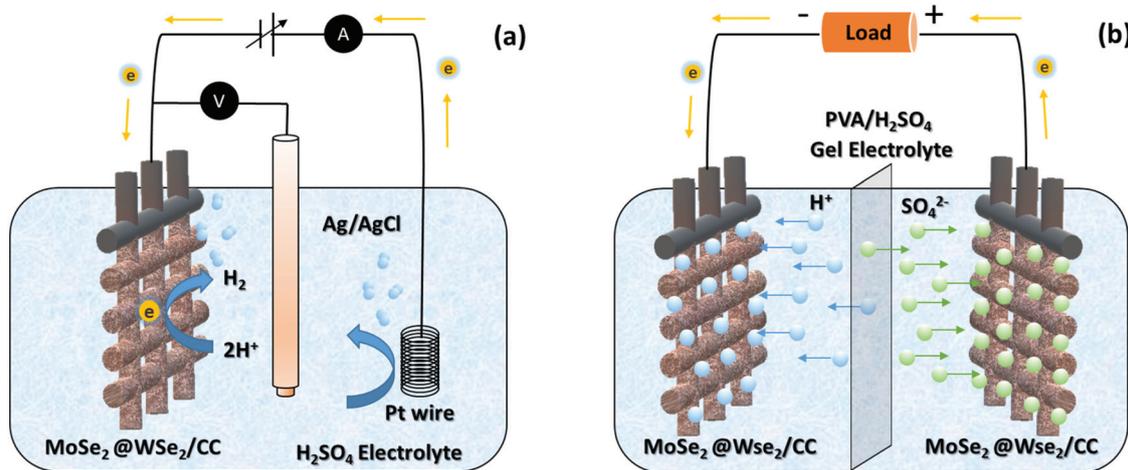


**Fig. 8** The schematic working mechanism of (a) hydrogen evolution and (b) FSSC-based on MoSe$_2$@WSe$_2$ HS composite on CC.

promoting electron transport, which increases the absorption and desorption rate of hydrogen (H$^+$) for HER activity. Moreover, the large electrochemically active surface area of the MoSe$_2$@WSe$_2$ HS with the electrolyte and at the same time carbon support as the electron transport pathway accelerates the diffusion rate of electrolyte ions acquiring extra capacitance and stability.[66,67] Direct liquid processing and high electrochemical performance of the MoSe$_2$@WSe$_2$ HS composite can be utilized to develop high performance and wearable energy devices.

## Conclusion

In conclusion, we have developed the MoSe$_2$@WSe$_2$ HS composite by a simple and direct deposition by electrophoresis as an efficient electrocatalyst for HER and supercapacitor application. The binder-free EPD approach provides several heterointerfaces between MoSe$_2$ and WSe$_2$ nanocrystals. Due to electronic modulation, MoSe$_2$@WSe$_2$ HS facilitated electron transport and a short diffusion channel for electrolyte ions at the solid–liquid interface. As predicted, the MoSe$_2$/WSe$_2$ HS catalyst achieves a lower overpotential of 158 mV, smaller Tafel slope of 46 mV dec$^{-1}$ for the current density of 10 mA cm$^{-2}$, and is stable for a long time. MoSe$_2$@WSe$_2$ HS demonstrated potential for FSSC with an excellent $C_{sp}$ of 401 F g$^{-1}$ at 1 A g$^{-1}$ and 97.20% capacitance retention after 5000 cycles with high flexible stability over 1000 bending cycles.

## Author contributions

Alkesh B. Patel: conceptualization, methodology, investigation, formal analysis, data curation, writing – original draft, writing – review & editing, visualization. Jayraj V. Vaghasiya: investigation, methodology, data Curation, writing – review & editing. Payal Chauhan: conceptualization, methodology, investigation, data curation, writing – review & editing. C. K. Sumesh: validation, resources, writing – review & editing. Vikas Patel: resources, data curation. Saurabh S. Soni: conceptualization, resources, writing – review & editing, supervision. K. D. Patel: conceptualization, methodology, writing – review & editing, supervision, project administration, visualization. Praveen Garg: resources, data curation. G. K. Solanki: visualization, supervision, writing – review & editing. V. M. Pathak: project administration, review & editing.

## Conflicts of interest

There are no conflicts to declare.

## Acknowledgements

## References

1 C. Jiang, S. J. A. Moniz, A. Wang, T. Zhang and J. Tang, *Chem. Soc. Rev.*, 2017, **46**, 4645–4660.

2 K. Eiler, S. Suriñach, J. Sort and E. Pellicer, *Appl. Catal., B*, 2020, **265**, 118597.

3 X. Zhao, Z. Zhang, X. Cao, J. Hu, X. Wu, A. Yun, R. Ng, G. Lu and Z. Chen, *Appl. Catal., B*, 2020, **260**, 118156.

4 F. Ma, L. Yu, C. Xu and X. W. Lou, *Energy Environ. Sci.*, 2016, **9**, 862–866.

5 A. B. Patel, P. Chauhan, K. Patel, C. K. Sumesh, S. Narayan, K. D. Patel, G. K. Solanki, V. M. Pathak, P. K. Jha and V. Patel, *ACS Sustainable Chem. Eng.*, 2020, **8**, 4809–4817.

6 P. Chauhan, G. K. Solanki, A. B. Patel, K. Patel, P. Pataniya, S. Narayan, K. D. Patel, P. K. Jha and V. M. Pathak, *Sol. Energy Mater. Sol. Cells*, 2019, **200**, 109936.

7 H. Li, X. Jia, Q. Zhang and X. Wang, *CHEMPR*, 2018, **4**, 1510–1537.

8 P. Chauhan, A. B. Patel, G. K. Solanki, K. D. Patel, V. M. Pathak, C. K. Sumesh, S. Narayan and P. K. Jha, *Appl. Surf. Sci.*, 2021, **536**, 147739.

9 A. B. Patel, P. Chauhan, H. K. Machhi, S. Narayan, C. K. Sumesh, K. D. Patel, S. S. Soni, P. K. Jha, G. K. Solanki and V. M. Pathak, *Phys. E*, 2020, **119**, 114019.

10 K. Zhang, Y. Li, S. Deng, S. Shen, Y. Zhang and G. Pan, *ChemElectroChem*, 2019, **6**, 3530–3548.

11 A. Eftekhari, *Appl. Mater. Today*, 2017, **8**, 1–17.

12 A. Eftekhari, *J. Mater. Chem. A*, 2017, **5**, 18299–18325.

13 H. Zhang, *ACS Nano*, 2015, **9**, 9451–9469.

14 S. R. Kadam, A. N. Enyashin, L. Houben, R. Bar-Ziv and M. Bar-Sadan, *J. Mater. Chem. A*, 2020, **8**, 1403–1416.

15 S. Hussain, K. Akbar, D. Vikraman, R. A. Afzal, W. Song, K. An, A. Farooq, J. Park, S. Chun and J. Jung, *Nanomaterials*, 2018, **8**, 929.

16 W. Liao, Y. Huang, H. Wang and H. Zhang, *Appl. Mater. Today*, 2019, **16**, 435–455.

17 C. K. Sumesh and S. C. Peter, *Dalton Trans.*, 2019, **48**, 12772–12802.

18 J. Su, G. D. Li, X. H. Li and J. S. Chen, *Adv. Sci.*, 2019, **6**, 1801702.

19 J. Yang, J. Zhu, J. Xu, C. Zhang and T. Liu, *ACS Appl. Mater. Interfaces*, 2017, **9**, 44550–44559.

20 S. Li, W. Zang, X. Liu, S. J. Pennycook, Z. Kou, C. Yang, C. Guan and J. Wang, *Chem. Eng. J.*, 2018, **359**, 1419–1426.

21 T. Wang, H. Jin, J. Li and Y. Wei, *Nanotechnology*, 2019, **30**, 015707.

22 G. Cunningham, M. Lotya, C. S. Cucinotta, S. Sanvito, S. D. Bergin, R. Menzel, M. S. P. Shaffer and J. N. Coleman, *ACS Nano*, 2012, 3468–3480.

23 A. B. Patel, H. K. Machhi, P. Chauhan, S. Narayan, V. Dixit, S., S. Soni, P. K. Jha, G. K. Solanki, K. D. Patel and V. M. Pathak, *ACS Appl. Mater. Interfaces*, 2019, **11**, 4093–4102.

24 K. K. Sonigara, H. K. Machhi, J. V. Vaghasiya, A. Gibaud, S. C. Tan and S. S. Soni, *Small*, 2018, **14**, 1800842.

25 Y. Ma, J. Han, M. Wang, X. Chen and S. Jia, *J. Mater.*, 2018, **4**, 108–120.

26 C. Jian, W. Hong, Q. Cai and W. Liu, *J. Mater. Chem. A*, 2021, **9**, 26113–26118.

27 Z. Liu, H. Zhao, N. Li, Y. Zhang, X. Zhang and Y. Du, *Inorg. Chem. Front.*, 2016, **3**, 313–319.

28 H. Zhang, J. Ji, A. A. Gonzalez and J. H. Choi, *J. Mater. Chem. C*, 2017, **5**, 1233–11238.

29 P. Martínez-Merino, E. Sani, L. Mercatelli, R. Alcántara and J. Navas, *ACS Sustainable Chem. Eng.*, 2020, **8**, 1627–1636.

30 A. Alam, G. Saeed and S. Lim, *J. Electroanal. Chem.*, 2020, **879**, 114775.

31 F. M. Pesci, M. Sokolikova, C. Grotta, P. C. Sherrell, F. Reale, K. Sharda, N. Ni, P. Palczynski and C. Mattevi, *ACS Catal.*, 2017, **7**, 4990–4998.

32 M. Y. A. Ismail, J. B. Malherbe, O. S. Odutemowo, E. G. Njoroge, T. T. Hlatshwayo, M. Mlambo and E. Wendler, *Vacuum*, 2018, **149**, 74–78.

33 H. Liu, S. Hussain, A. Ali, B. A. Naqvi, D. Vikraman, W. Jeong, W. Song, K. S. An and J. Jung, *RSC Adv.*, 2018, **8**, 25514–25518.

34 Y. Tao, O. De Luca, B. Singh, A. J. Kamphuis, J. Chen, P. Rudolf and P. P. Pescarmona, *Mater. Today Chem.*, 2020, **18**, 100373.

35 K. Si, J. Ma, C. Lu, Y. Zhou, C. He, D. Yang, X. Wang and X. Xu, *Appl. Surf. Sci.*, 2020, **507**, 145082.

36 C. Liu, Y. Qiu, F. Wang, K. Wang, Q. Liang and Z. Chen, *Adv. Mater. Interfaces*, 2017, **4**, 1700681.

37 G. Han, Y. Liu, W. Hu, B. Dong, X. Li and Y. Chai, *Mater. Chem. Phys.*, 2015, **167**, 271–277.

38 R. Koutavarapu, C. V. Reddy, B. Babu, K. R. Reddy, M. Cho and J. Shim, *Int. J. Hydrogen Energy*, 2020, **45**, 7716–7740.

39 G. Zhao, K. Rui, S. X. Dou and W. Sun, *Adv. Funct. Mater.*, 2018, **28**, 1803291.

40 B. Wang, K. Zhao, Z. Yu, C. Sun, Z. Wang, N. Feng, L. Mai, Y. Wang and Y. Xia, *Energy Environ. Sci.*, 2020, **13**, 2200–2208.

41 W. Li, G. Liu, J. Li, Y. Wang, L. Ricardez-Sandoval, Y. Zhang and Z. Zhang, *Appl. Surf. Sci.*, 2019, **498**, 143869.

42 D. Vikraman, A. A. Arbab, S. Hussain, N. K. Shrestha, S. H. Jeong, J. Jung, S. A. Patil and H. S. Kim, *ACS Sustainable Chem. Eng.*, 2019, **7**, 13195–13205.

43 Y. Chen, J. Zhang, P. Guo, H. Liu, Z. Wang, M. Liu, T. Zhang, S. Wang, Y. Zhou, X. Lu and J. Zhang, *ACS Appl. Mater. Interfaces*, 2018, **10**, 27787–27794.

44 X. Wang, B. Zheng, B. Yu, B. Wang, W. Hou, W. Zhang and Y. Chen, *J. Mater. Chem. A*, 2018, **6**, 7842–7850.

45 Z. Chen, W. Wang, S. Huang, P. Ning, Y. Wu, C. Gao, T. T. Le, J. Zai, Y. Jiang, Z. Hu and X. Qian, *Nanoscale*, 2020, **12**, 326–335.

46 B. Wang, Z. Wang, X. Wang, B. Zheng, W. Zhang and Y. Chen, *J. Mater. Chem. A*, 2018, **6**, 12701–12707.

47 D. Vikraman, S. Hussain, K. Karuppasamy, A. Feroze, A. Kathalingam, A. Sanmugam, S. H. Chun, J. Jung and H. S. Kim, *Appl. Catal., B*, 2020, **264**, 118531.

48 W. Guo, Q. Van Le, H. H. Do, A. Hasani and M. Tekalgne, *Appl. Sci.*, 2019, **9**, 5035.

49 P. Wu, G. Sun, Y. Chen, W. Xu, H. Zheng, J. Xu, L. Wang and D. L. Peng, *Nanoscale Res. Lett.*, 2020, **15**, 132.

50 Y. Huang, H. Lu, H. Gu, J. Fu, S. Mo, C. Wei, Y. E. Miao and T. Liu, *Nanoscale*, 2015, **7**, 18595–18602.

51 D. Vikraman, S. Hussain, L. Truong, K. Karuppasamy and H. Kim, *Appl. Surf. Sci.*, 2019, **480**, 611–620.

52 M. Cai, F. Zhang, C. Zhang, C. Lu, Y. He, Y. Qu, H. Tian, X. Feng and X. Zhuang, *J. Mater. Chem. A*, 2017, **6**, 138–144.

53 Y. Qiu, X. Li, M. Bai, H. Wang, D. Xue, W. Wang and J. Cheng, *Inorg. Chem. Front.*, 2017, **4**, 675–682.

54 V. Shrivastav, S. Sundriyal, P. Goel, V. Shrivastav, U. K. Tiwari and A. Deep, *Electrochim. Acta*, 2020, **345**, 136194.

55 J. V. Vaghasiya, C. C. Mayorga-martinez and M. Pumera, *Chem. Soc. Rev.*, 2020, **49**, 7819–7844.

56 X. Gao, L. Yin, L. Zhang, Y. Zhao and B. Zhang, *Chem. Eng. J.*, 2020, **395**, 125058.

57 S. J. Patil and D. W. Lee, *J. Mater. Chem. A*, 2018, **6**, 9592–9603.

58 B. Pandit, L. K. Bommineedi and B. R. Sankapal, *J. Energy Chem.*, 2018, **31**, 79–88.

59 X. Yang, J. Li, C. Hou, Q. Zhang and Y. Li, *Front. Chem.*, 2020, **8**, 442.

60 X. Zhou, Y. Ren, Y. Lu, Z. Cheng, W. Wang and Q. Wang, *Adv. Mater. Interfaces*, 2019, **6**, 1–8.

61 W. Chen, T. Wei, L. Mo, S. Wu and Z. Li, *Chem. Eng. J.*, 2020, **15**, 125856.

62 P. Yu, W. Fu, Q. Zeng, J. Lin, C. Yan, Z. Lai and B. Tang, *Adv. Mater.*, 2017, **29**, 1701909.

63 M. S. Javed, S. Shoaib, A. Shah and S. Hussain, *Chem. Eng. J.*, 2019, **15**, 122814.

64 S. S. Karade and B. R. Sankapal, *J. Electroanal. Chem.*, 2017, **802**, 131–138.

65 Y. Zhao, X. He, R. Chen and Q. Liu, *Int. J. Hydrogen Energy*, 2019, **44**, 13690–13699.

66 C. Guan, X. Liu, W. Ren, X. Li, C. Cheng and J. Wang, *Adv. Energy Mater.*, 2017, **7**, 1602391.

67 X. Wang, H. Li, H. Li, S. Lin, W. Ding, X. Zhu, Z. Sheng, H. Wang, X. Zhu and Y. Sun, *Adv. Funct. Mater.*, 2020, **30**, 0190302.